

Banner appropriate to article type will appear here in typeset article

# Turbulent Prandtl number from isotropically forced turbulence

Petri J. Käpylä<sup>1</sup> †, and Nishant K. Singh<sup>2</sup>

<sup>1</sup>Institute for Astrophysics and Geophysics, Göttingen University, Friedrich-Hund-Platz 1, 37077 Göttingen, Germany

<sup>2</sup>Inter-University Centre for Astronomy and Astrophysics, Post Bag 4 Ganeshkhind, Savitribai Phule Pune University Campus, Pune 411 007, India

(Received xx; revised xx; accepted xx)

Turbulent motions enhance the diffusion of large-scale flows and temperature gradients. Such diffusion is often parameterized by coefficients of turbulent viscosity ( $\nu_t$ ) and turbulent thermal diffusivity ( $\chi_t$ ) that are analogous to their microscopic counterparts. We compute the turbulent diffusion coefficients by imposing large-scale velocity and temperature gradients on a turbulent flow and measuring the response of the system. We also confirm our results using experiments where the imposed gradients are allowed to decay. To achieve this, we use weakly compressible three-dimensional hydrodynamic simulations of isotropically forced homogeneous turbulence. We find that the turbulent viscosity and thermal diffusion, as well as their ratio the turbulent Prandtl number,  $Pr_t = \nu_t/\chi_t$ , approach asymptotic values at sufficiently high Reynolds and Peclet numbers. We also do not find a significant dependence of  $Pr_t$  on the microscopic Prandtl number  $Pr = \nu/\chi$ . These findings are in stark contrast to results from the  $k - \epsilon$  model which suggests that  $Pr_t$  increases monotonically with decreasing  $Pr$ . The current results are relevant for the ongoing debate of, for example, the nature of the turbulent flows in the very low  $Pr$  regimes of stellar convection zones.

**Key words:** Turbulence

## 1. Introduction

The fluids in stellar convection zones are generally characterized by a low microscopic Prandtl number,  $Pr = \nu/\chi$ , where  $\nu$  is the kinematic viscosity and  $\chi$  is the thermal diffusivity (e.g. Ossendrijver 2003; Augustson *et al.* 2019). Typical values in the bulk of the solar convection zone, for example, range between  $10^{-6}$  and  $10^{-3}$  (Schumacher & Sreenivasan 2020). Recently, several studies have explored the possibility that solar convection operates at a high effective Prandtl number regime, meaning that the turbulent Prandtl number  $Pr_t$  exceeds unity (e.g. O'Mara *et al.* 2016; Bekki *et al.* 2017; Karak *et al.* 2018), as a possible solution to the too high velocity amplitudes in simulations in comparison to the Sun (e.g. Hanasoge *et al.* 2012; Schumacher & Sreenivasan 2020). However, few attempts have been

† Email address for correspondence: pkaepyl@uni-goettingen.de

made to actually measure the turbulent Prandtl number from simulations. A notable exception is the study of [Pandey \*et al.\* \(2021\)](#) who reported that the turbulent Prandtl number decreases steeply as a function of the molecular Prandtl number such that  $\text{Pr}_t \propto \text{Pr}^{-1}$  in simulations of standard Boussinesq and variable heat conductivity Boussinesq convection.

Here we set out to measure turbulent viscosity and thermal diffusivity from a simpler system of isotropically forced homogeneous turbulence. This is done by imposing large-scale gradients of velocity and temperature (equivalently specific entropy) and measuring the response of the system. The turbulent diffusion coefficients are computed from the Boussinesq ansatz and an analogous expression for the enthalpy flux. This method provides a direct measurement of the diffusion coefficients without the need to resort to turbulent closures. Similar methods were used recently to measure the turbulent magnetic Prandtl number ([Käpylä \*et al.\* 2020](#)). We compare our results with those from the widely used  $k - \epsilon$  model which was also used by [Pandey \*et al.\* \(2021\)](#). We show that the direct results and those from the  $k - \epsilon$  model are systematically different and that the latter yields misleading results.

## 2. The model

We model isotropically forced, non-isothermal, turbulence in a fully periodic cube of volume  $(2\pi)^3$ . We solve the equations of fully compressible hydrodynamics

$$\frac{D \ln \rho}{Dt} = -\nabla \cdot \mathbf{u}, \quad (2.1)$$

$$\frac{D\mathbf{u}}{Dt} = -\frac{1}{\rho}(\nabla p - \nabla \cdot 2\nu\rho\mathbf{S}) + \mathbf{f} - \frac{1}{\tau}(\mathbf{u} - \bar{\mathbf{u}}_0), \quad (2.2)$$

$$T \frac{Ds}{Dt} = -\frac{1}{\rho}(\nabla \cdot \mathcal{F}_{\text{rad}} - C) + 2\nu\mathbf{S}^2 - \frac{T}{\tau}(s - \bar{s}_0), \quad (2.3)$$

where  $D/Dt = \partial/\partial t + \mathbf{u} \cdot \nabla$  is the advective derivative,  $\rho$  is the density,  $\mathbf{u}$  is the velocity,  $p$  is the pressure,  $\nu$  is the kinematic viscosity,  $\mathbf{S}$  is the traceless rate-of-strain tensor with

$$S_{ij} = \frac{1}{2}(u_{i,j} + u_{j,i}) - \frac{1}{3}\delta_{ij}\nabla \cdot \mathbf{u}, \quad (2.4)$$

$\mathbf{f}$  is the external forcing,  $\tau$  is a relaxation timescale, and  $\bar{\mathbf{u}}_0$  is the target mean velocity profile. Furthermore,  $T$  is the temperature,  $s$  is the specific entropy,  $\mathcal{F}_{\text{rad}}$  is the radiative flux,  $C$  is a cooling term, and  $\bar{s}_0$  is the target mean specific entropy profile. Radiation is modeled via the diffusion approximation, with the radiative flux given by

$$\mathcal{F}_{\text{rad}} = -c_P\rho\chi\nabla T, \quad (2.5)$$

where  $c_P$  is the specific heat in constant pressure and  $\chi$  is the thermal diffusivity. The ideal gas equation of state  $p = (c_P - c_V)\rho T = \mathcal{R}\rho T$  is assumed, where  $\mathcal{R}$  is the gas constant, and  $c_V$  is the specific heat capacity at constant volume. In the presence of an imposed large-scale flow, viscous dissipation of kinetic energy acts as a source for thermal energy and leads to a linear increase of the temperature. Additional volumetric cooling is applied to counter this with

$$C(\mathbf{x}) = \rho c_P \frac{T(\mathbf{x}) - \langle T_0 \rangle}{\tau_{\text{cool}}}, \quad (2.6)$$

where  $\langle T_0 \rangle$  is the volume-averaged initial temperature and  $\tau_{\text{cool}}$  is a cooling timescale. We use  $\tau = \tau_{\text{cool}} = (c_{s0}k_1)^{-1}$ , where  $c_{s0}$  is the initial uniform value of the sound speed and  $k_1$  is the wavenumber corresponding to the box scale.

The external forcing is given by (see [Brandenburg 2001](#))

$$\mathbf{f} = \text{Re}\{N(t)\mathbf{f}_{\mathbf{k}(t)} \exp[i\mathbf{k}(t) \cdot \mathbf{x} - i\phi(t)]\}, \quad (2.7)$$

where  $\mathbf{x}$  is the position vector and  $N(t) = f_0 c_s(k(t)c_s/\delta t)^{1/2}$  is a normalization factor where  $f_0$  is the forcing amplitude,  $k = |\mathbf{k}|$ ,  $\delta t$  is the length of the time step, and  $-\pi < \phi(t) < \pi$  is a random delta-correlated phase. The vector  $\mathbf{f}_{\mathbf{k}}$  describes non-helical transverse waves, and is given by

$$\mathbf{f}_{\mathbf{k}} = \frac{\mathbf{k} \times \hat{\mathbf{e}}}{\sqrt{k^2 - (\mathbf{k} \cdot \hat{\mathbf{e}})^2}}, \quad (2.8)$$

where  $\hat{\mathbf{e}}$  is an arbitrary unit vector, and where the wavenumber  $\mathbf{k}$  is randomly chosen. The target profiles of mean velocity and specific entropy are given by

$$\bar{\mathbf{u}}_0 = u_0 \sin(k_1 z) \hat{\mathbf{e}}_y, \quad (2.9)$$

$$\bar{s}_0 = s_0 \sin(k_1 z). \quad (2.10)$$

In addition to the physical diffusion, the advective terms in (2.1) to (2.3) are implemented in terms of fifth-order upwinding derivatives with sixth-order hyperdiffusive corrections and flow-dependent diffusion coefficients; see Appendix B of [Dobler et al. \(2006\)](#).

The PENCIL CODE ([Pencil Code Collaboration et al. 2021](#))<sup>†</sup>, which uses high-order finite differences for spatial and temporal discretisation, was used to produce the numerical simulations.

### 2.1. Units, system parameters, and diagnostics

The equations are non-dimensionalized by choosing the units

$$[x] = k_1^{-1}, \quad [\rho] = \rho_0, \quad [u] = c_{s0}, \quad [s] = c_P, \quad (2.11)$$

where  $\rho_0$  is the initial uniform density and  $c_{s0} = \sqrt{\gamma \mathcal{R} T_0}$  is the sound speed corresponding to the initial temperature  $T_0$ . The level of velocity fluctuations is determined by the forcing amplitude  $f_0$  along with the kinematic viscosity. A key system parameter is the ratio of kinematic viscosity and thermal diffusion or the Prandtl number

$$\text{Pr} = \frac{\nu}{\chi}, \quad (2.12)$$

which is varied between 0.01 and 10 in the present study. The Reynolds and Péclet numbers quantify the level of turbulence of the flows:

$$\text{Re} = \frac{u_{\text{rms}}}{\nu k_f}, \quad \text{Pe} = \text{PrRe} = \frac{u_{\text{rms}}}{\chi k_f}, \quad (2.13)$$

where  $u_{\text{rms}} = \sqrt{\langle (\mathbf{u} - \bar{\mathbf{u}}_0)^2 \rangle}$  is the volume-averaged fluctuating rms-velocity and  $k_f$  is the average forcing wavenumber characterizing the energy injection scale. The latter is chosen from a uniformly distributed narrow range in the vicinity of  $5k_1$ . The imposed gradients of large-scale flow and entropy are quantified by

$$\text{Ma}_s = \frac{u_0}{c_{s0}}, \quad \text{Ma}_g = \frac{[(\gamma - 1)s_0 T_0]^{1/2}}{c_{s0}}, \quad (2.14)$$

<sup>†</sup> <http://github.com/pencil-code>

Set	Pr	Re	Pe	Ma	Ma <sub>s</sub>	Ma <sub>g</sub>	# runs
i001	0.01	27 ... 779	0.27 ... 7.8	0.069 ... 0.079	0.01 ... 0.03	0.07 ... 0.1	10
i002	0.02	27 ... 779	0.54 ... 16	0.069 ... 0.080	0.01 ... 0.03	0.07 ... 0.1	12
i005	0.05	27 ... 780	1.4 ... 39	0.069 ... 0.080	0.01 ... 0.03	0.07 ... 0.1	12
i010	0.1	12 ... 800	1.2 ... 80	0.060 ... 0.082	0.01 ... 0.03	0.07 ... 0.1	30
i020	0.2	27 ... 781	5.4 ... 156	0.069 ... 0.080	0.01 ... 0.03	0.07 ... 0.1	10
i025	0.25	397	99	0.081	0.01 ... 0.03	0.07 ... 0.1	2
i050	0.5	27 ... 781	14 ... 390	0.069 ... 0.081	0.01 ... 0.03	0.07 ... 0.1	12
i075	0.75	399	301	0.081	0.01 ... 0.03	0.07 ... 0.1	2
i100	1.0	27 ... 1582	27 ... 1582	0.069 ... 0.081	0.01 ... 0.03	0.07 ... 0.1	14
i200	2.0	22	44	0.068	0.01 ... 0.03	0.07 ... 0.1	2
i500	5.0	22.2	111	0.068	0.01 ... 0.03	0.07 ... 0.1	2
i1000	10.0	22.3	223	0.068	0.01 ... 0.03	0.07 ... 0.1	2
du001	0.01	153	1.5	0.078	0.01	–	10
du010	0.1	153 ... 391	15 ... 39	0.078	0.01 ... 0.03	–	11
du100a	1.0	154	154	0.079	0.01	–	10
du100b	1.0	154	154	0.079	0.03	–	10
ds001	0.01	153	1.5	0.078	–	0.1	10
ds010	0.1	153 ... 391	15 ... 39	0.078	–	0.07 ... 0.1	11
ds100	1.0	153	153	0.078	–	0.1	10

Table 1: Summary of runs. Runs with imposed velocity or specific entropy gradients are denoted with prefix i, whereas decay experiments of velocity (specific entropy) are identified by prefix du (ds). Grid resolutions range between  $144^3$  and  $1152^3$ .

where  $Ma_s$  is the Mach number of the mean flow and  $k_U = k_s = k_1$ . The Mach number of the turbulent flow is given by

$$Ma = \frac{u_{rms}}{\langle c_s \rangle}, \quad (2.15)$$

where  $\langle c_s \rangle$  is the volume-averaged speed of sound.

Mean values are taken to be horizontal averages denoted by overbars, that is

$$\bar{f} = \frac{1}{(2\pi)^2} \int_x \int_y f(\mathbf{x}) dx dy. \quad (2.16)$$

Often an additional time average over the statistically steady part of the simulation is taken. Volume averages are denoted by angle brackets  $\langle \cdot \rangle$  apart from the rms-values which are always assumed to be volume-averaged unless otherwise stated. Errors were estimated by dividing the time series in three parts and averaging over each subinterval. The greatest deviation from the average computed over the whole time series was taken as the error estimate.

### 3. Results

The simulations discussed in the present study are listed in table 1.

#### 3.1. Turbulent viscosity and heat diffusion from imposed flow and entropy methods

We measure the turbulent viscosity and thermal diffusivity in two ways. First, we impose sinusoidal large-scale profiles of velocity (2.9) or entropy (2.10). The response of the system are non-zero Reynolds stress and vertical enthalpy flux profiles that are parameterized with gradient diffusion terms (e.g. Rüdiger 1989)

$$F_z^{\text{enth}}(z) = c_P \overline{(\rho u_z)' T'} \approx c_P \bar{\rho} \overline{u_z' T'} = -\chi_i \bar{\rho} \bar{T} \frac{\partial \bar{s}}{\partial z}, \quad (3.1)$$

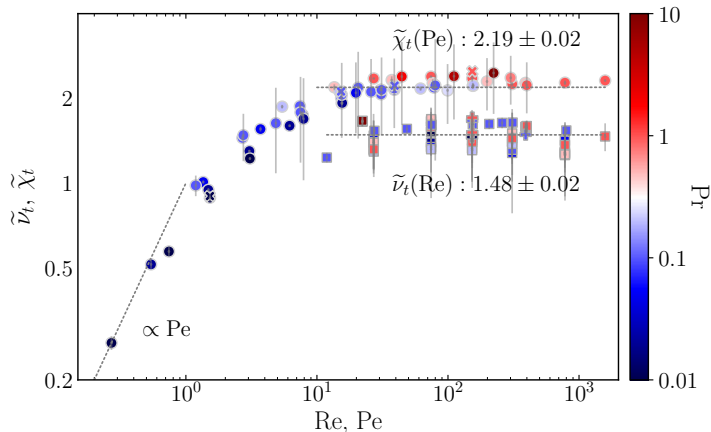


Figure 1: Normalized turbulent viscosity  $\tilde{\nu}_t = \nu_t/\nu_{t0}$  (squares) and heat diffusivity  $\tilde{\chi}_t = \chi_t/\chi_{t0}$  (circles) as functions of Reynolds and Péclet numbers. The crosses ( $\times$ ) and pluses ( $+$ ) indicate results from decay experiments. The colours of the symbols indicate the microscopic Prandtl number as shown by the colourbar. The dotted horizontal lines show fit to the data for  $Pe, Re > 10$  and a line proportional to  $Pe$  is shown for low  $Pe$ .

and

$$R_{yz}(z) = \overline{u'_y u'_z} = -\nu_t \frac{\partial \bar{u}_y}{\partial z}, \quad (3.2)$$

where primes denote fluctuations from the mean, e.g.,  $\mathbf{u}' = \mathbf{u} - \bar{\mathbf{u}}$ . The Mach number in the current simulations is always less than 0.1. Therefore we neglect density-dependent terms in our analysis because they scale with  $Ma^2$ .

The coefficients  $\chi_t$  and  $\nu_t$  are assumed to be scalars and were obtained from linear fits between time-averaged  $F_z^{\text{enth}}$  and  $\overline{\rho T \partial_z \bar{s}}$  and between  $R_{yz}$  and  $\partial_z \bar{u}_y$ , respectively. Results from our simulations are shown in figure 1. We normalize  $\nu_t$  and  $\chi_t$  by

$$\nu_{t0} = \chi_{t0} = \frac{1}{3} u_{\text{rms}} k_f^{-1}, \quad (3.3)$$

which is an order of magnitude estimate for the turbulent diffusion coefficients. We note that in the parameter regimes studied here, the estimates  $\nu_{t0}$  and  $\chi_{t0}$  are very similar in all of our runs. Our results show that for low Péclet numbers the turbulent heat diffusion increases in proportion to  $Pe$  for  $Pe \lesssim 1$ . This is consistent with earlier numerical results for turbulent viscosity (e.g. Käpylä *et al.* 2020), magnetic diffusivity (e.g. Sur *et al.* 2008), and passive scalar diffusion (Brandenburg *et al.* 2009), and with corresponding analytic results in the diffusion dominated ( $Pe \ll 1$ ) regime. For sufficiently large  $Pe$ ,  $\tilde{\chi}_t$  tends to a constant value. The turbulent viscosity is also roughly constant in the parameter space covered here. For low fluid Reynolds numbers  $\nu_t$  is proportional to  $Re$  as has been shown in Käpylä *et al.* (2020). However, we do not cover this parameter regime with the current simulations.

### 3.2. Turbulent viscosity and heat diffusion from decay experiments

Decay experiments were made as an independent way to measure the turbulent viscosity and heat diffusion. Snapshots from the imposed velocity/entropy gradient runs were used as initial conditions and the relaxation terms of the rhs of the Navier–Stokes and entropy equations were deactivated. The large-scale velocity and entropy profiles in such runs decay due to the combined effect of molecular and turbulent diffusion. To measure the decay rate

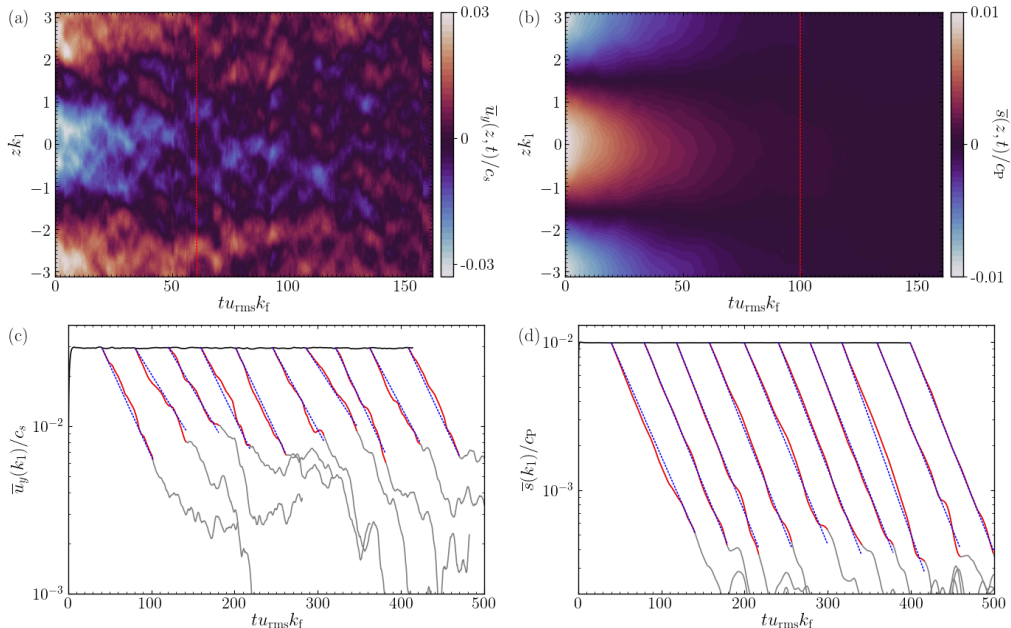


Figure 2: Panels (a) and (b):  $\bar{u}_y(t, z)$  and  $\bar{s}(t, z)$  normalized by  $c_s$  and  $c_p$ , respectively, from decay experiments with  $Pr = 1$  and  $Re = 157$ . Red vertical lines denote end times of exponential fits. Panels (c) and (d): temporal decays of  $k_z/k_1 = 1$  mode of  $\bar{u}_y$  and  $\bar{s}$ , respectively; black line shows the progenitor run, and the red/gray lines indicate the decaying runs; red part is used to fit exponential decay; blue dotted lines show the exponential fit.

we monitored the amplitude of the  $k = k_1$  components of  $\bar{u}_y$  and  $\bar{s}$ . Exponential decay laws

$$\bar{u}_y(t, k_1) = \bar{u}_y(t_0, k_1)e^{-(\nu_t + \nu)s t}, \quad \bar{s}(t, k_1) = \bar{s}(t_0, k_1)e^{-(\chi_t + \chi)s t}, \quad (3.4)$$

were then fitted to the numerical data. Representative examples from decay experiments of large-scale velocity and entropy are shown in figure 2. The upper panels (a) and (b) show  $\bar{u}_y(z, t)$  and  $\bar{s}(z, t)$  from typical decay experiments. The  $k_1$  components of these fields decay exponentially when the forcing is turned off; see panels (c) and (d) of figure 2. Ultimately the amplitude of the  $k_1$  mode decreases sufficiently such that it cannot be distinguished from the background turbulence. The time it takes to reach this state varies and depends on the initial amplitudes  $u_0$  and  $s_0$ . However, at the same time these amplitudes need to be kept as low as possible to avoid non-linear effects becoming important (see, e.g. Käpylä *et al.* 2020). This is particularly important for the velocity field due to which the range from which turbulent viscosity can be estimated is limited which necessitates running several experiments with different snapshots as initial conditions to reach converged values for  $\nu_t$  and  $\chi_t$ .

Due to this, only a limited subset of the parameter range covered by the imposed cases were repeated with decay experiments. We used ten snapshots from each run for the decay experiments. The separation between the snapshots is roughly  $\Delta t = 40u_{rms}k_f$  such that the realizations can be considered uncorrelated. Results from the decay experiments are shown in figure 1 with crosses ( $\chi_t$ ) and pluses ( $\nu_t$ ). We find that the results from the decay experiments are consistent with those from the imposed flow and entropy gradient methods.

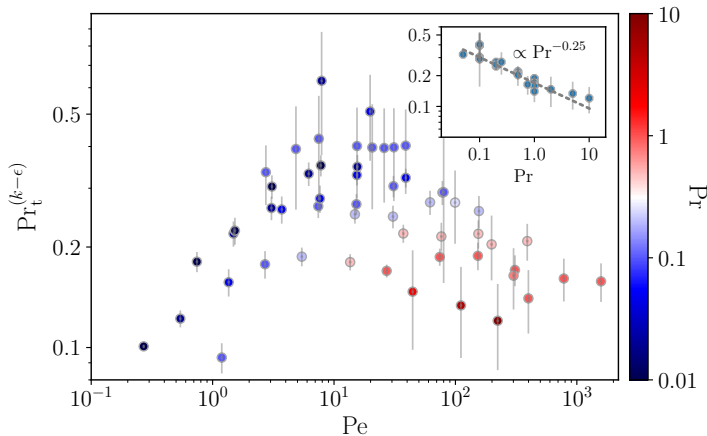


Figure 3: Turbulent Prandtl number  $\text{Pr}_t^{(k-\epsilon)}$  according to (3.7) as a function of Péclet number. The colour of the symbols denotes the molecular Prandtl number as indicated by the colour bar. Inset:  $\text{Pr}_t^{(k-\epsilon)}$  versus  $\text{Pr}$  from runs with  $\text{Pe} > 20$ .

### 3.3. The $k - \epsilon$ model

To facilitate a comparison with Pandey *et al.* (2021) we use the expressions of  $\nu_t$  and  $\chi_t$  derived under the  $k - \epsilon$  model with

$$\nu_t^{(k-\epsilon)} = c'_\nu k_u^2 / \epsilon_K, \quad (3.5)$$

$$\chi_t^{(k-\epsilon)} = c'_\chi k_u k_T / \epsilon_T, \quad (3.6)$$

where  $k_u = \langle \mathbf{u}'^2 \rangle / 2$  is the turbulent kinetic energy,  $k_T = \langle T'^2 \rangle$  is the variance of the temperature fluctuations,  $c'_\nu$  and  $c'_\chi$  are assumed to be universal constants<sup>†</sup>. Viscous and thermal dissipation rates are defined as  $\epsilon_K = 2\nu[\langle \mathbf{S}^2 \rangle - \langle \mathbf{S}_0 \rangle^2]$  and  $\epsilon_T = \chi \langle (\nabla T')^2 \rangle = \chi[\langle (\nabla T)^2 \rangle - \langle (\nabla \bar{T})^2 \rangle]$ , respectively, where we have removed contributions from the mean flow and the mean entropy;  $\mathbf{S}_0$  denotes the traceless rate-of-strain tensor as defined in (2.4) but with  $\bar{\mathbf{u}}_0$  instead of  $\mathbf{u}$ . Pandey *et al.* (2021) computed  $\text{Pr}_t$  using the  $k - \epsilon$  model by fixing the ratio of  $c'_\nu / c'_\chi$ , which yields

$$\text{Pr}_t^{(k-\epsilon)} = \frac{\nu_t^{(k-\epsilon)}}{\chi_t^{(k-\epsilon)}} = \frac{c'_\nu k_u \epsilon_T}{c'_\chi k_T \epsilon_u}. \quad (3.7)$$

For simplicity, we assume  $c'_\nu / c'_\chi = 1$  in this subsection. The results are shown in figure 3. We find that taking the ratio  $c'_\nu / c'_\chi$  to be a constant leads to results where  $\text{Pr}_t^{(k-\epsilon)}$  increases monotonically with decreasing  $\text{Pr}$  when  $\text{Pe}$  is larger than about 20; see the inset in figure 3 which reveals a dependence of  $\text{Pr}^{-0.25}$ . Qualitatively, this result is in agreement with the one in Pandey *et al.* (2021). However, we would like to note here that a strong assumption was made to reach this conclusion, namely, that the ratio  $c'_\nu / c'_\chi$  is fixed, and that  $c'_\nu$  and  $c'_\chi$  are universal constants, independent of control parameters such as  $\text{Re}$  and  $\text{Pe}$ . Henceforth, we relax these assumptions, and also omit primes from the coefficients  $c_\nu$  and  $c_\chi$ .

<sup>†</sup> Primes indicate the constancy of  $c'_\nu$  and  $c'_\chi$ , but see section 3.4 where this assumption is lifted.

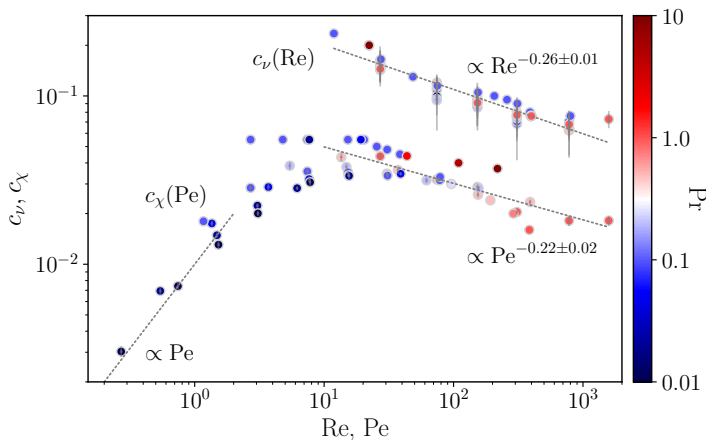


Figure 4: Similar to figure 1 but for  $c_v(\text{Re})$  and  $c_\chi(\text{Pe})$  from (3.8) and (3.9). The colours again indicate the microscopic Prandtl number. The grey dotted lines indicate fits to the data for  $(\text{Pe}, \text{Re} > 10)$  and a line proportional to  $\text{Pe}$  is shown for low  $\text{Pe}$ .

### 3.4. Relaxing the assumption that $c_v$ and $c_\chi$ are constants

It is reasonable to assume that for sufficiently large Reynolds and Péclet numbers  $k_u$  and  $k_T$  tend to constant values. Furthermore, there is evidence from numerical simulations that  $\epsilon_K$  also tends to a non-zero constant value for large Reynolds numbers. Similar evidence for  $\epsilon_T$  has not been presented. Therefore it is not clear whether the assumption of universality of  $c_v$  and  $c_\chi$  is valid. This is particularly important for numerical simulations such as those in the current study where the Reynolds and Péclet numbers are still modest. Since we have independently measured  $\nu_t$  and  $\chi_t$  using the imposed flow and entropy method (section 3.1) and from decay experiments (section 3.2), we can estimate  $c_v$  and  $c_\chi$  using:

$$c_v = \nu_t / (k_u^2 / \epsilon_K), \quad (3.8)$$

$$c_\chi = \chi_t / (k_u k_T / \epsilon_T), \quad (3.9)$$

where  $\nu_t$  and  $\chi_t$  are the ones obtained above in section 3.1 with the imposed field method. The results are shown in figure 4. Our results indicate that  $c_v$  and  $c_\chi$  are highly variable and that they depend not only on  $\text{Re}$  and  $\text{Pe}$  but also on  $\text{Pr}$ . Furthermore, for sufficiently large Reynolds and Péclet numbers,  $c_v$  and  $c_\chi$  show decreasing trends proportional to roughly  $-0.25$  power of  $\text{Re}$  and  $\text{Pe}$ , respectively. This shows that any estimate of  $\nu_t$  or  $\chi_t$  with the  $k - \epsilon$  model in the parameter regime studied here would require prior knowledge of  $c_v$  and  $c_\chi$  for the particular parameters  $(\text{Re}, \text{Pe}, \text{Pr})$  of that system.

### 3.5. Turbulent Prandtl number

Our results for the turbulent Prandtl number

$$\text{Pr}_t = \frac{\nu_t}{\chi_t} \quad (3.10)$$

are shown in figure 5 with  $\nu_t$  and  $\chi_t$  as discussed in sections 3.1 and 3.2. We find that for  $\text{Pe} \lesssim 1$  the turbulent Prandtl number is roughly inversely proportional to  $\text{Pe}$  for low molecular Prandtl number. We have not computed the turbulent Prandtl number for cases where both  $\text{Re}$  and  $\text{Pe}$  are smaller than unity. For sufficiently high Péclet number the turbulent Prandtl number tends to a constant value which is close to 0.7. This is in accordance with theoretical estimates in that  $\text{Pr}_t$  is somewhat smaller than unity. For example, Rüdiger (1989) derived



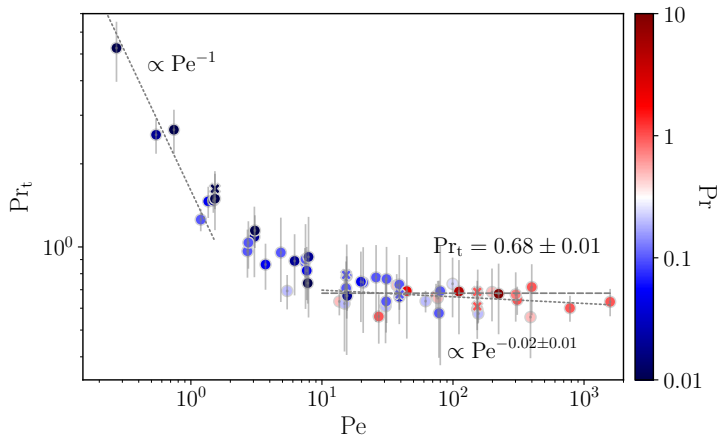


Figure 5: Turbulent Prandtl number  $Pr_t = \nu_t/\chi_t$  as a function of Péclet number. The colour of the symbols denotes the molecular Prandtl number as indicated by the colour bar. The crosses (x) show results from decay experiments. Linear and power law fits to data for  $Pe > 10$  are shown by the dashed and dotted lines, respectively, and a line proportional to  $Pe^{-1}$  is shown for low  $Pe$ .

$Pr_t = 2/5$  using first-order smoothing approximation. The turbulent Prandtl number plays an important role also in the atmospheric boundary layer where several methods yield values of the order of unity (Li 2019, and references therein).

That, the turbulent Prandtl number  $Pr_t$  reaches a constant value at sufficiently large  $Pe$ , independent of  $Pr$ , is in stark contrast to the results obtained from the  $k - \epsilon$  model with a fixed  $c_\nu/c_\chi$ ; compare figures 3 and 5. Now we make an attempt to understand the reason for this discrepancy. From figure 4 we note the following approximate scaling relations at sufficiently large  $Re$  and  $Pe$ :  $c_\nu \propto Re^{-0.25}$  and  $c_\chi \propto Pe^{-0.25}$ , suggesting thus that the ratio  $c_\nu/c_\chi$  scales with the Prandtl number as  $Pr^{+0.25}$ . With this, if we let  $c'_\nu/c'_\chi \propto Pr^{+0.25}$  in 3.7, instead of a fixed ratio, and note from the inset of figure 3 that the factor  $k_u \epsilon_T / k_T \epsilon_u \propto Pr^{-0.25}$ , we would obtain from 3.7 that  $Pr_t^{(k-\epsilon)}$  becomes independent of  $Pr$ , agreeing thus qualitatively with our results as shown in figure 5. Therefore we conclude that the results from the  $k - \epsilon$  model with a fixed value for the ratio  $c_\nu/c_\chi$  are unreliable and that the strong dependence of  $Pr_t$  on  $Pr$  found in Pandey *et al.* (2021) is due to the restrictive assumption in their model.

#### 4. Conclusions

Using simulations of weakly compressible isotropically forced turbulence with imposed large-scale gradients of velocity and temperature, and corresponding decay experiments, we find that the turbulent Prandtl number  $Pr_t$  is roughly 0.7 and independent of the microscopic Prandtl number  $Pr$  provided that the Péclet number is higher than about ten. This is in stark contrast from the recent results of Pandey *et al.* (2021) who found that  $Pr_t \propto Pr^{-1}$  from non-Boussinesq simulations of convection. Although the physical setups are quite different, we were able to qualitatively reproduce their finding under the strong assumption that  $c_\nu/c_\chi$  is fixed, and note that the method by which the turbulent viscosity and thermal diffusivity were obtained in Pandey *et al.* (2021) produce unreliable results even in the simpler cases considered here. Relaxing their assumption of universality of  $c_\nu$  and  $c_\chi$ , we find that these depend not only on  $Re$  and  $Pe$ , respectively, but also on  $Pr$ . This allows us to understand the reason for the discrepancy.

**Acknowledgments.** We thank S. Sridhar for his comments on an earlier draft of the manuscript. NS thanks the hospitality provided by RRI, Bangalore where parts of this work were done. We gratefully acknowledge the use of high performance computing facilities at HLRN in Göttingen and Berlin, and IUCAA, Pune.

**Funding.** This work was supported by the Deutsche Forschungsgemeinschaft Heisenberg programme (P.J.K., grant number KA4825/4-1).

**Declaration of interests.** The authors report no conflict of interest.

**Author ORCID.** P. J. Käpylä, <https://orcid.org/0000-0001-9619-0053>; N. K. Singh, <https://orcid.org/0000-0001-6097-688X>.

**Author contributions.** Both authors contributed equally to running the simulations, analyzing data, reaching conclusions, and in writing the paper.

## REFERENCES

- AUGUSTSON, K. C., BRUN, A. S. & TOOMRE, J. 2019 Rossby and Magnetic Prandtl Number Scaling of Stellar Dynamos. *ApJ* **876** (1), 83.
- BEKKI, Y., HOTTA, H. & YOKOYAMA, T. 2017 Convective Velocity Suppression via the Enhancement of the Subadiabatic Layer: Role of the Effective Prandtl Number. *ApJ* **851**, 74, arXiv: 1711.05960.
- BRANDENBURG, A. 2001 The Inverse Cascade and Nonlinear Alpha-Effect in Simulations of Isotropic Helical Hydromagnetic Turbulence. *ApJ* **550**, 824–840, arXiv: arXiv:astro-ph/0006186.
- BRANDENBURG, A., SVEDIN, A. & VASIL, G. M. 2009 Turbulent diffusion with rotation or magnetic fields. *MNRAS* **395**, 1599–1606, arXiv: 0901.2112.
- DOBLER, W., STIX, M. & BRANDENBURG, A. 2006 Magnetic Field Generation in Fully Convective Rotating Spheres. *ApJ* **638**, 336–347, arXiv: arXiv:astro-ph/0410645.
- HANASOGE, S. M., DUVAL, T. L. & SREENIVASAN, K. R. 2012 Anomalously weak solar convection. *Proc. Natl. Acad. Sci.* **109**, 11928–11932, arXiv: 1206.3173.
- KÄPYLÄ, P. J., RHEINHARDT, M., BRANDENBURG, A. & KÄPYLÄ, M. J. 2020 Turbulent viscosity and magnetic Prandtl number from simulations of isotropically forced turbulence. *A&A* **636**, A93, arXiv: 1901.00787.
- KARAK, B. B., MIESCH, M. & BEKKI, Y. 2018 Consequences of high effective Prandtl number on solar differential rotation and convective velocity. *Physics of Fluids* **30** (4), 046602, arXiv: 1801.00560.
- LI, DAN 2019 Turbulent prandtl number in the atmospheric boundary layer - where are we now? *Atmospheric Research* **216**, 86–105.
- O’MARA, B., MIESCH, M. S., FEATHERSTONE, N. A. & AUGUSTSON, K. C. 2016 Velocity amplitudes in global convection simulations: The role of the Prandtl number and near-surface driving. *Adv. Space Res.* **58**, 1475–1489, arXiv: 1603.06107.
- OSSENDRIJVER, M. 2003 The solar dynamo. *A&A Rev.* **11**, 287–367.
- PANDEY, AMBRISH, SCHUMACHER, JÖRG & SREENIVASAN, KATEPALLI R. 2021 Non-Boussinesq convection at low Prandtl numbers relevant to the Sun. *Physical Review Fluids* **6** (10), 100503, arXiv: 2108.04472.
- PENCIL CODE COLLABORATION, BRANDENBURG, AXEL, JOHANSEN, ANDERS, BOURDIN, PHILIPPE, DOBLER, WOLFGANG, LYRA, WLADIMIR, RHEINHARDT, MATTHIAS, BINGERT, SVEN, HAUGEN, NILS, MEE, ANTONY, GENT, FREDERICK, BABKOVSKAIA, NATALIA, YANG, CHAO-CHIN, HEINEMANN, TOBIAS, DINTRANS, BORIS, MITRA, DHURBADITYA, CANDELARESI, SIMON, WARNECKE, JÖRN, KÄPYLÄ, PETRI, SCHREIBER, ANDREAS, CHATTERJEE, PIYALI, KÄPYLÄ, MAARIT, LI, XIANG-YU, KRÜGER, JONAS, AARNES, JØRGEN, SARSON, GRAEME, OISHI, JEFFREY, SCHOBER, JENNIFER, PLASSON, RAPHAËL, SANDIN, CHRISTER, KARCHNIWY, EWA, RODRIGUES, LUIZ, HUBBARD, ALEXANDER, GUERRERO, GUSTAVO, SNODIN, ANDREW, LOSADA, ILLA, PEKKILÄ, JOHANNES & QIAN, CHENGENG 2021 The Pencil Code, a modular MPI code for partial differential equations and particles: multipurpose and multiuser-maintained. *The Journal of Open Source Software* **6** (58), 2807.
- RÜDIGER, G. 1989 *Differential Rotation and Stellar Convection. Sun and Solar-type Stars*. Berlin: Akademie Verlag.
- SCHUMACHER, JÖRG & SREENIVASAN, KATEPALLI R. 2020 Colloquium: Unusual dynamics of convection in the Sun. *Reviews of Modern Physics* **92** (4), 041001.
- SUR, S., BRANDENBURG, A. & SUBRAMANIAN, K. 2008 Kinematic  $\alpha$ -effect in isotropic turbulence simulations. *MNRAS* **385**, L15–L19, arXiv: 0711.3789.